ON THE EFFECT OF FREE-STREAM TURBULENCE ON THE AERODYNAMIC DRAG AND WAKE DYNAMICS OF AN AHMED BODY

Pierre-Yves Passaggia, Nicolas Mazellier, Azeddine Kourta
University of Orléans, INSA-CVL, PRISME, EA 4229, 45072, Orléans, France
pierre-yves.passaggia@univ-orleans.fr

1 ABSTRACT

We report an extensive experimental investigation on the effect of inflow turbulence on a square-back Ahmed body. Variations reaching up to $+16\%$ and -17% of the drag coefficient are observed for free-stream turbulence representative of open-road conditions (Saunders & Mansour, 2000). Regular turbulence grids are mounted upstream the body and turbulence intensity together with the integral length scale of turbulence are varied using different mesh, bar sizes, and solidity. The role of free-stream turbulence on the drag coefficient and the wake meandering dynamics is investigated. In particular, the statistics associated with the dynamics of the reflectional symmetry breaking of the wake are analysed using a proper orthogonal decomposition method. Increasing free-stream turbulence leads to a drastic change in the meandering dynamics of the wake which evolves from intermittent to essentially Gaussian. Interestingly, the amplitude, the frequency of the meandering and the spatial distribution of the wake are found to decrease when increasing free-stream turbulence. Wake meandering is shown to be strongly receptive to free-stream turbulence. More importantly, we draw a link between the receptivity of the shear-layer instabilities and the wake meandering which hints to important conclusions in the scope of flow-control strategies.

2 Introduction

The transportation industry, and in particular, road vehicles, remains one of the main contributors to global energy consumption and pollutant emissions. Car manufacturers must therefore comply with environmental regulations such as CO_2-emissions standards which are becoming increasingly strict. Reducing the aerodynamic drag through flow control strategies stands as an appealing solution to comply with these policies. Heavy commercial vehicles are considered aerodynamically inefficient compared to other ground vehicles due to their unstreamlined body shapes. A large commercial vehicle travelling at 100 km/h consumes about approximately 52% of the total fuel to provide power to overcome the aerodynamic drag (Schoon & Pan, 2007). The aerodynamic drag of a semi-trailer truck typically accounts for about 75-80% of the total drag for a driving speed of 100 km/h (Hucho, 1998). It is therefore of the utmost importance to understand the dynamics of such wakes to free-stream turbulence in order to establish robust flow-control methods. Over the past two decades, substantial efforts have been invested to control the vehicle wake, which is characterised by both large pressure drag and three-dimensional (3D) coherent structures (Hucho & Sovran, 1993). Altogether, these phenomena contribute in large parts to performance losses and make the physical mechanisms at play extremely complex (Bonnavion et al., 2017). Although significant drag reduction was reported at the laboratory scale using either passive or active control methods (see e.g., Pujals et al., 2010; Barros et al., 2016; McNally et al., 2019; Lorite-Díez et al., 2020, to only cite a few), these achievements were obtained in operating conditions which are far from being representative of real-life applications, which evolve in strongly turbulent upwind.

The role of external conditions on the aerodynamics of vehicles and in particular the near wake remains largely unexplored because of the facilities required to run such large-scale experiments. Most of the previously cited studies took place in *low*-free-stream turbulence intensities $T_u \approx 0.5\%$, which are at least one order of magnitude lower than values observed in open-road conditions where T_u varies between 2% and 15% (Watkins & Saunders, 1995; Saunders & Mansour, 2000). Higher turbulence intensities may even be found in heavy traffic and/or wind gusts conditions. Moreover, the on-road integral lengthscale (L_u), which can be seen as the dimension of the energy-containing eddies, of the incoming flow ranges between $0.3H$ (with other cars) and $3.5H$ (open-road and light winds) where H is the typical height of the tested vehicles (Saunders & Mansour, 2000). In this study, the effect of free-stream turbulence on the near-wake meandering is investigated for nearly isotropic and homogeneous turbulence conditions.

3 Experimental setup

The bluff body is a full-scale square-back Ahmed body with dimensions $[L, W, H] = [1.044, 0.340, 0.288]$ m (Ahmed et al. (1984)). Experiments were carried out in the S1 wind tunnel at PRISME laboratory (Orléans, France). The test section of this closed-loop wind tunnel is a 2×2 m^2 square and extends over 5 m. The ground clearance G was set to $G = 50$ mm and a flap is mounted along the trailing edge of the raised floor (see figure 1(a)). The investigated free-stream velocity, monitored by a Pitot probe located at 2m from the grids, is $U_\infty = 25 \pm 0.2$ m/s, which corresponds to $Re_H = U_\infty H / \nu \approx 4.8 \times 10^5$, with ν the kinematic viscosity of air. Free-stream turbulence is generated by regular bi-planar grids placed at the inlet of the test section (1.5 m upstream of the leading edge of the raised floor). In this study, eight grids with square bars were considered, each of them being characterised by a solidity defined as $\chi = b/M(2 - b/M)$ where M and b stand for the grid mesh and the bar thickness, respectively. The grid properties are summarised in Passaggia et al. (2021).
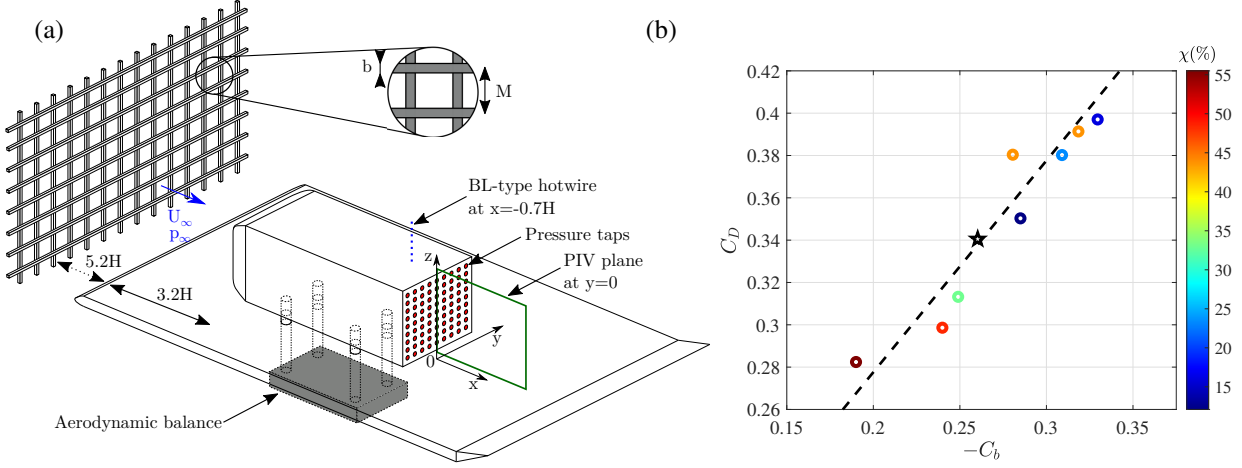
Figure 1. (a) Experimental setup showing the pressure taps (red circles), PIV plane (green rectangle), and positions of the streamwise velocity profiles measured by a BL-type hot-wire probe. (b) C_D as a function of C_b for all cases including the reference case denoted by a pentagram.

Grid ref.	$b/H(\%)$	M/H	$\chi(\%)$	L_u/H	$T_u(\%)$	C_b	C_D	$ln(G)$	N	A
No Grid	/	/	/	/	0.5	-0.260	0.341	0.0204	164	6.40
B25M10	8.68	0.35	43.8	20	4.77	-0.319	0.391	0.0218	173	6.95
B25M20	8.68	0.69	23.4	10	5.58	-0.309	0.380	0.0187	232	6.56
B25M30	8.68	1.04	16.0	6.6	5.56	-0.330	0.397	0.0207	94	6.96
B25M40	8.68	1.39	12.1	5	5.13	-0.285	0.313	0.0192	304	6.55
B58M32	20.1	1.10	33.0	6.25	8.72	-0.249	0.350	0.0121	232	5.94
B70M26	24.3	0.97	43.7	7.7	10.16	-0.280	0.384	0.0172	322	6.00
B90M32	31.2	1.10	48.3	6.25	11.04	-0.240	0.299	0.0080	1094	5.06
B120M36	41.7	1.25	55.5	5.6	12.90	-0.190	0.282	0.0042	1489	4.37

Table 1. Summary of main physical parameters covered in this study. Free-stream turbulence characteristics are measured at $x = 11.4H$ from the grid.

4 Free-stream turbulence and drag

The Ahmed body is linked to a six-components strain gauge balance through its feet, avoiding any contact with the ground. We focus here on the drag force F_D and the yaw F_y, the coefficients of which are $C_D = 2F_D/(\rho U_\infty^2 S)$ and $C_y = 2F_y/(\rho U_\infty^2 S)$, where ρ is the air density and $S = HW$ the frontal area. The drag coefficient is measured with a 2% precision and is well within the range reported in the literature for a similar geometry and flow condition (Volpe *et al.*, 2015; Lucas *et al.*, 2017). Note that the mean side forces are nearly null and that the lift coefficient is also one order of magnitude lower, as reported in Passaggia *et al.* (2021). Pressure distributions over the rear surface S are measured through 81 pressure taps connected to three Chell MicroDAQ pressure scanners recording pressure fluctuations at 50 Hz. The pressure taps are identified in figure 1(a) by red circles. The acquisition frequency was set to 50 Hz and allowed for measuring the dynamics of meandering wake. In addition, 5 Kulite pressure sensors we mounted near the four corners of the body to measure pressure fluctuations at a frequency of 1 kHz as well as an additional one located at the centre of the body. The pressure coefficient is defined as $C_p = 2(P - P_\infty)/(\rho U_\infty^2)$ where P and P_∞ are the wall pressure and the static pressure measured

in the free-stream by the Pitot tube, respectively. The precision of the pressure scanner is given with a 1.6% accuracy, which corresponds to an error bar equivalent to the size of the points used in figure 1(b). The resulting base pressure coefficient is $C_b = \frac{1}{HW} \int_S C_p(y,z)dS$. Note that the values of C_D and C_b for the reference case are slightly different than previously reported in Volpe *et al.* (2015) because the position of the Pitot tube was different than in their experiment which was located at $x = 8.4H$ from the grid.

Varying the characteristics of turbulence in the freestream (i.e. varying χ) modifies the base pressure coefficient C_b and the drag coefficients C_D with a linear relation (see figure 1(b)) where the linear regression provides $C_D \approx -C_b + 0.078$, as shown in figure 1(b) which is in agreement with previous studies (Lorite-Díez *et al.*, 2020; Haffner *et al.*, 2021). These relations therefore point to the strong sensitivity of the flow to free-stream turbulence and in particular, the drag coefficient, which is essentially controlled by the pressure at the base. In turn, base pressure is known to be controlled by both the geometry of the wake and the Reynolds stresses (Grandemange *et al.*, 2012). Since the Reynolds stresses were already analysed in Passaggia *et al.* (2021), we tie a first link between the wake stability and
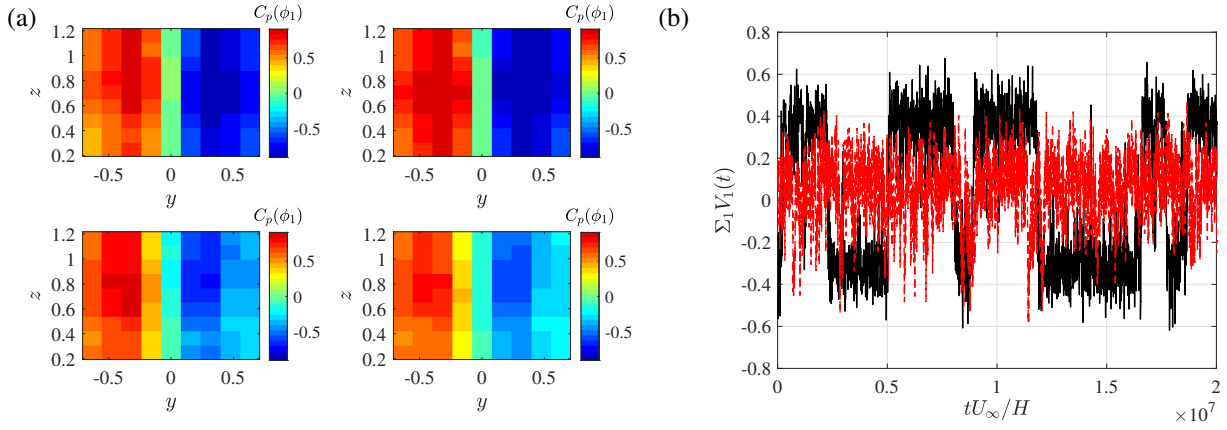
Figure 2. (a) Contours of pressure coefficient for the second POD mode $U_2(y,z)\sqrt{\Sigma_2}$ for $\chi = 0$ (reference, top left), $\chi = 43.8\%$ (largest drag increase, top right), $\chi = 33.0\%$ (mild drag decrease, bottom left), $\chi = 55\%$ (largest drag decrease, bottom right). (b) Sample temporal evolution of the second POD mode $V_2(t)\sqrt{\Sigma_2}$ for the reference case ($\chi = 0$) and the strongest free-stream turbulent condition ($\chi = 55\%$).
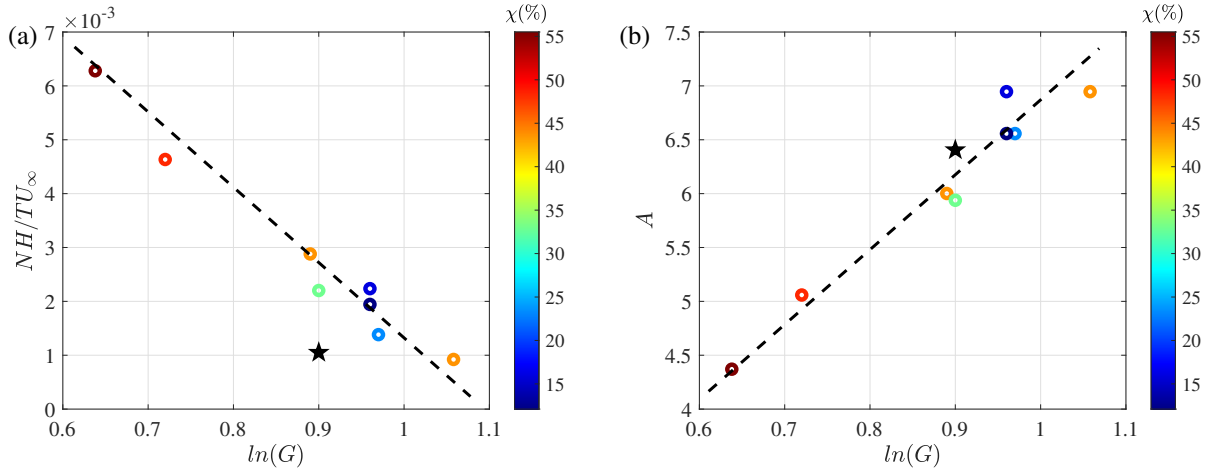

Figure 3. (a) Non-dimensional switching frequency NH/TU_∞ as a function of the spatial growth rate of shear-layer instabilities $ln(G)$. (b) RSB mode amplitude $A = \sqrt{\Sigma_2}$ also reported as a function of $ln(G)$. The black pentagram reports the reference case, without grid.

the loss of symmetry caused by the so-called reflectional symmetry breaking mode which drives the meandering of the wake.

5 Wake meandering dynamics

The meandering of the wake is analysed by means of a modal decomposition based on modes computed through a Proper Orthogonal Decomposition (POD). These modes are later used to split the pressure fluctuations between a mean, the RSB mode, and the remainder from the shear layer modes and incoherent fluctuations. In particular, we show that the RSB mode is essentially controlled by the mean-flow properties. The intermittent dynamics of the shear-layer modes and incoherent fluctuations are analysed through their statistics.

5.1 POD modes dynamics

The dynamics of the the wake are known to be driven by an RSB mode which switches between the left and the right side of the wake, reported in several studies (Volpe *et al.*, 2015; Grandemange *et al.*, 2012). While the instability dynamics of the upper shear layer was recently reported in Passaggia *et al.*

(2021) together with its contribution to the drag, we investigate the wake meandering which is known to induce a large drag decrease when the wake switches between each possible side (i.e. left or right in the present case (Haffner *et al.*, 2020)). In order to carry out this analysis, we use 81 pressure sensors located on the flat back of the body using a proper orthogonal decomposition such that

$$C_p(y,z,t) = \sum_i U_i(y,z)\, \Sigma_i\, V_i(t), \qquad (1)$$

where $U_i(x_i)$ is the spatial distribution of the ith POD mode, while Σ_i and $V_i(t)$ represent the energy and the temporal evolution of the ith POD modes, respectively. Note that **U** and **V** are orthonormal matrices while Σ is a diagonal matrix. Note that here, the first mode is the mean base pressure while the second mode is always associated with the RSB mode, whatever the level of free-stream turbulence.

The spatial distribution of the POD modes for different turbulence grids is shown in Figure 2(a). The pressure associated with the RSB mode is found to be either slightly increased for the grid with the smaller mesh size (i.e. the smaller turbulence intensity and the smaller integral lengthscale) while it
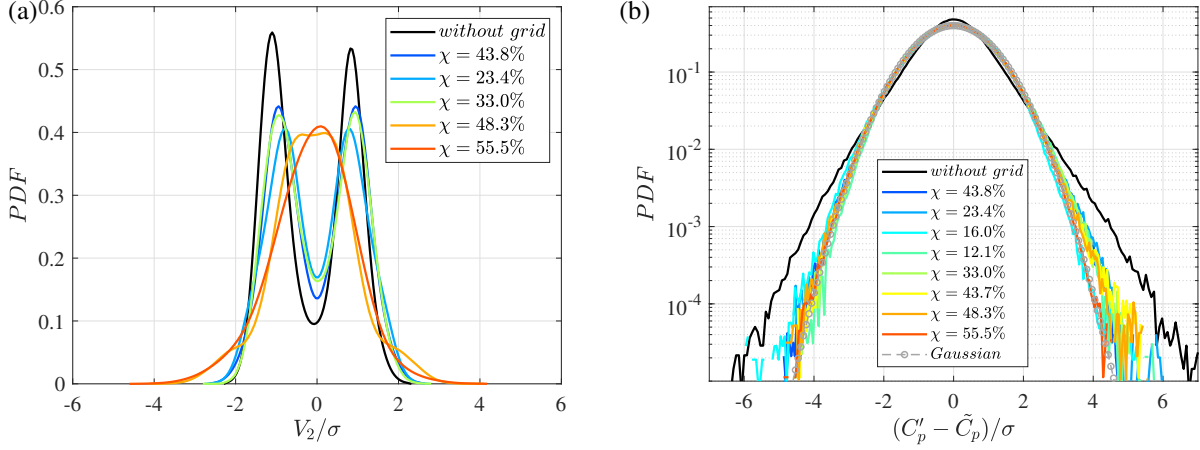
Figure 4. (a) Probability density functions of the RSB mode temporal dynamics $\Sigma_2 V_2(t)$. Note that all PDFs were normalised with their density. (b) Probability density functions of the high-pass dynamics $C'_p - \tilde{C}_p$ where $\tilde{C}_p$ is computed using a moving average with a window of 0.1 s, extracted from the Kulite sensors located near the roof. The PDFs are normalised with respect to their integral while the width is rescaled using the variance of the signals.

is clearly decreased when the bar and the mesh size increase. However, it is interesting to note that the pressure signature of the mode is only weakly affected by free-stream turbulence, even for the stronger free-stream turbulence conditions. Figure 2(b) shows the temporal evolution of the second POD mode for the case without grid. It is compared with the temporal evolution for the largest turbulence grid where the amplitude is clearly decreased and where the number of switches has also increased.

The characteristic non-dimensional number of switches per unit time between each state NH/TU_∞, is shown in Figure 3(a) and is the related to inverse of the mean residence time on either the left or the right side of body's flat back. Here, N is the number of switches recorded by the pressure scanner through the temporal evolution of the mode $V_2(t)$ while T is the recording time which was set to half an hour. In the worst case scenario, more than 90 switches were still recorded which provides a good convergence of the statistics. The amplitude of the modes is shown in Figure 3(b) where the amplitude $A = \sqrt{\Sigma_2}$ is found to either increase or decrease depending on the characteristics of the free-stream turbulence. This result was very recently reported in Burton *et al.* (2021) for different turbulence grid arrangements which may not lead to homogeneous and isotropic free-stream turbulent conditions. However, nor the mean residence time, nor the amplitude of the reflectional symmetry breaking mode seems to scale with the drag coefficient. However, we show that both the amplitude of the wake and the mean switching time scale linearly with the growth rate of the Kelvin-Helmholtz instabilities originating from the wake Passaggia *et al.* (2021).

As recently shown in Haffner *et al.* (2020), the switch between the left and the right state is caused by a set of Kelvin-Helmholtz modes located in the shear layer. The stability of the shear layer was recently investigated in Passaggia *et al.* (2021). The shear-layer modes were found to be be associated with Strouhal numbers in the range $St = [0.1,1]$. The same modes where also identified in Haffner *et al.* (2020) and caused the switch between the left and the right state of the RSB mode. As shown in Passaggia *et al.* (2021), it is the receptivity of the shear layer to free-stream turbulence that controls these shear-layer modes and the amplitude of these modes is found to be controlled by the energy gain of the dominant instability given

by $ln(G)$, where G is the spatial energy gain of the shear-layer modes Passaggia *et al.* (2021).

Both the RSB mode amplitude and the non-dimensional switching frequency are found to scale linearly with the growth rate of the shear-layer instabilities (i.e. see Figure 3) which hints to the receptivity of free-stream turbulence by the the shear layers.

5.2 POD modes and pressure-fluctuations statistics

Next, we analyse the statistics of the fluctuations where the dynamics are now split in a triple decomposition between the mean base pressure, the RSB mode, and the remainder of the pressure fluctuations. This decomposition writes

$$C_p(y,z,t) = \overline{C_p}(y,z) + \tilde{C}_p(y,z,t) + C''_p(y,z,t), \quad (2)$$

where $\overline{C_p}(y,z) = U_1(y,z)\Sigma_1 = C_b$, $\tilde{C}_p(y,z,t) = U_1(y,z)\Sigma_2 V_2(t)$. Figure 4(a) shows the probability density function associated with the RSB mode dynamics $\sqrt{\Sigma_2}V_2(t)$ for different turbulent free-stream conditions. For the reference case without free-stream turbulence, the PDF is essentially symmetric and shows two= distinct peaks which correspond to the left and right states associated with the RSB mode. As free-stream turbulence increases, the amplitude of the peaks progressively decreases and both peaks tend to merge. For the larger values of free-stream turbulence, the PDF evolves towards a Gaussian, particularly visible for $\chi = 55\%$. This result is important as it shows that for $Tu > 10\%$ and $L_u \approx H$, the meandering of the wake is strongly affected by the dynamics of the free-stream turbulence which is indeed Gaussian for scales in the range of the integral lengthscale.

This is also visible in the dynamics of the $C''_p(y,z,t)$ measured near the roof, on the back of the body using the fast Kulite sensors. Figure 4(b) reports the statistics of the shear-layer modes and the incoherent dynamics given by $C''_p(y,z,t)$. For the reference case, without free-stream turbulence, the PDF is clearly not Gaussian. The tails of the PDF extend by two standard deviations when compared with the Gaussian reference. The tails are the trace of the shear-layer fluctuations as shown in Haffner *et al.* (2020) leading to the switching of the

mode from one side to the other, whence its intermittent nature.

As free-stream turbulence increases, the tails of the PDFs quickly narrow, even for $T_u < 5\%$, and approach the Gaussian distribution. For the largest grid, fluctuations fit nearly perfectly the Gaussian distribution, which further hints to the fact that the shear-layer display a strong receptivity to free-stream dynamics and thus, the meandering, together with the shear-layer modes and the incoherent fluctuations.

These results hint to the fact that the dynamics of the wake are further influenced when increasing free-stream turbulence and that the shear-layer receptivity is an important mechanism in explaining the wake dynamics of bluff bodies in turbulent free streams.

6   Conclusions and outlook

The near-wake dynamics of an Ahmed body and aerodynamic characteristics are analysed and compared for different turbulence grids positioned upstream the body. It is shown that free-stream turbulence strongly modifies the drag coefficient and thus the mean flow. We then address the role of the wake meandering which is the most energetic structure in the wake and which has been long speculated to play an important in controlling drag. Although, free-stream turbulence is found to be of key importance for controlling wake meandering and the shear-layer dynamics, a clear link between drag and meandering is not clear. On the other hand, free-stream turbulence plays a key role in controlling the unsteady aerodynamic in bluff-body wakes as shown by the dynamics of the first Proper Orthogonal Decomposition (POD) mode, associated with the reflectional symmetry breaking (RSB) of the wake. Free-stream turbulence is found to have little influence on the structure of the pressure associated with the RSB mode on the base of the body. However, the dynamics and the amplitude of the mode is strongly affected. Increasing free-stream turbulence, the non-dimensional frequency of the RSB mode substantially increases while its amplitude follows a net decrease. The statistics of the RSB mode are also found to evolve from a Probability Density Function (PDF) with two peaks which merge and evolve towards a Gaussian-type PDF. The remainder of the pressure fluctuations are also analysed and while the dynamics of the shear layer are clearly non-Gaussian without free-stream turbulence, the intermittency disappears and the pressure fluctuations become essentially Gaussian, hinting to the strong receptivity of wake meandering and shear-layer instabilities with increasing free-stream turbulence.

These results hint to important conclusions when investigating flow control strategies of bluff-body wakes. A possible alley to perform flow control could aim at injecting turbulence all around the base of the body, with a turbulence intensity larger than 15% that extends far into the wake, its shear layer, and a turbulent Gaussian-type forcing.

Acknowledgements

REFERENCES

Ahmed, S. R., Ramm, G. & Faltin, G. 1984 Some salient features of the time-averaged ground vehicle wake. *SAE Trans.* pp. 473–503.

Barros, D., Borée, J., Noack, B. R., Spohn, A. & Ruiz, T. 2016 Bluff body drag manipulation using pulsed jets and coanda effect. *J. Fluid Mech.* **805**, 422–459.

Bonnavion, G., Cadot, O., Évrard, A., Herbert, V., Parpais, S., Vigneron, R. & Délery, J. 2017 On multistabilities of real car's wake. *J. Wind Eng. Ind. Aerodynamics* **164**, 22–33.

Burton, D, Wang, S, Smith, D Tudball, Scott, HN, Crouch, TN & Thompson, MC 2021 The influence of background turbulence on ahmed-body wake bistability. *Journal of Fluid Mechanics* **926**.

Grandemange, M., Gohlke, M., Parezanović, V. & Cadot, O. 2012 On experimental sensitivity analysis of the turbulent wake from an axisymmetric blunt trailing edge. *Phys. Fluids* **24** (3), 035106.

Haffner, Y., Borée, J., Spohn, A. & Castelain, T. 2020 Mechanics of bluff body drag reduction during transient near-wake reversals. *J. Fluid Mech* **894** (A14).

Haffner, Y., Castelain, T., Borée, J. & Spohn, A. 2021 Manipulation of three-dimensional asymmetries of a turbulent wake for drag reduction. *J. Fluid Mech.* **912**.

Hucho, W. & Sovran, G. 1993 Aerodynamics of road vehicles. *Ann. Rev. Fluid Mech.* **25** (1), 485–537.

Hucho, W.-H. 1998 Aerodynamics of road vehicles, society of automotive engineers. *Inc., Warrendale, PA* .

Lorite-Díez, M., Jiménez-González, J. I., Pastur, L., Martínez-Bazán, C. & Cadot, O. 2020 Experimental analysis of the effect of local base blowing on three-dimensional wake modes. *J. Fluid Mech* **883**.

Lucas, J.-M., Cadot, O., Herbert, V., Parpais, S. & Délery, J. 2017 A numerical investigation of the asymmetric wake mode of a squareback ahmed body–effect of a base cavity. *J. Fluid Mech.* **831**, 675–697.

McNally, J., Mazellier, N., Alvi, F. & Kourta, A. 2019 Control of salient flow features in the wake of a 25° ahmed model using microjets. *Exp. Fluids* **60** (1), 7.

Passaggia, Pierre-Yves, Mazellier, Nicolas & Kourta, Azeddine 2021 Aerodynamic drag modification induced by free-stream turbulence effects on a simplified road vehicle. *Physics of Fluids* **33** (10), 105108.

Pujals, G., Depardon, S. & Cossu, C. 2010 Drag reduction of a 3d bluff body using coherent streamwise streaks. *Exp. Fluids* **49** (5), 1085–1094.

Saunders, J. W. & Mansour, R. B. 2000 On-road and wind tunnel turbulence and its measurement using a four-hole dynamic probe ahead of several cars. *SAE Trans.* pp. 477–496.

Schoon, R. & Pan, F. P. 2007 Practical devices for heavy truck aerodynamic drag reduction. *Tech. Rep.*. SAE Technical Paper.

Volpe, R., Devinant, P. & Kourta, A. 2015 Experimental characterization of the unsteady natural wake of the full-scale square back Ahmed body: flow bi-stability and spectral analysis. *Exp. Fluids* **56** (5).

Watkins, S. & Saunders, J. W. 1995 Turbulence experienced by road vehicles under normal driving conditions. *Tech. Rep.*. SAE Technical Paper.